

# A numerical stability analysis for the Einstein-Vlasov system

Sebastian Günther\*, Jacob Körner†, Timo Lebeda‡, Bastian Pötzl\*,  
Gerhard Rein\*, Christopher Straub\*, Jörg Weber§

September 18, 2020

## Abstract

We investigate stability issues for steady states of the spherically symmetric Einstein-Vlasov system numerically in Schwarzschild, maximal areal, and Eddington-Finkelstein coordinates. Across all coordinate systems we confirm the conjecture that the first binding energy maximum along a one-parameter family of steady states signals the onset of instability. Beyond this maximum perturbed solutions either collapse to a black hole, form heteroclinic orbits, or eventually fully disperse. Contrary to earlier research, we find that a negative binding energy does not necessarily correspond to fully dispersing solutions. We also comment on the so-called turning point principle from the viewpoint of our numerical results. The physical reliability of the latter is strengthened by obtaining consistent results in the three different coordinate systems and by the systematic use of dynamically accessible perturbations.

## 1 Introduction

We consider in the context of general relativity a large ensemble of mass points which interact only through the gravitational field which they create collectively. Such a self-gravitating collisionless gas is used in astrophysics to model galaxies or globular clusters. Gravity is described by the Einstein equations

$$G_{\alpha\beta} = 8\pi T_{\alpha\beta}, \quad (1.1)$$

---

\*Department of Mathematics, University of Bayreuth, Germany

†Institute of Mathematics, Julius-Maximilians-Universität Würzburg, Germany

‡Department of Physics, University of Bayreuth, Germany

§Centre for Mathematical Sciences, Lund University, Sweden

where  $G_{\alpha\beta}$  is the Einstein tensor induced by the Lorentzian metric  $g_{\alpha\beta}$  with signature  $(- + + +)$  on the smooth spacetime manifold  $M$ , and  $T_{\alpha\beta}$  is the energy-momentum tensor given by the matter content of the spacetime. Greek indices run from 0 to 3, and we choose units in which the speed of light and the gravitational constant are equal to 1. The evolution equation for a collisionless gas is the collisionless Boltzmann or Vlasov equation so that we obtain the Einstein-Vlasov system. We study this system under the assumption that the spacetime is spherically symmetric and asymptotically flat, but we first formulate it in general.

The world line of a test particle on  $M$  obeys the geodesic equation

$$\dot{x}^\alpha = p^\alpha, \quad \dot{p}^\alpha = -\Gamma_{\beta\gamma}^\alpha p^\beta p^\gamma,$$

where  $x^\alpha$  denote general coordinates on  $M$ ,  $p^\alpha$  are the corresponding canonical momenta,  $\Gamma_{\beta\gamma}^\alpha$  are the Christoffel symbols induced by the metric  $g_{\alpha\beta}$ , the dot indicates differentiation with respect to proper time along the world line of the particle, and the Einstein summation convention is applied. We assume that all the particles in the ensemble have the same rest mass, normalized to 1, and move forward in time, i.e., their number density  $f$  is a non-negative function supported on the mass shell

$$PM := \left\{ g_{\alpha\beta} p^\alpha p^\beta = -1, \quad p^\alpha \text{ future pointing} \right\},$$

a submanifold of the tangent bundle  $TM$  of the spacetime manifold  $M$  which is invariant under the geodesic flow. Letting Latin indices range from 1 to 3 we choose coordinates  $(t, x^a)$  such that on the mass shell  $PM$  the variable  $p^0$  becomes a function of the remaining variables  $(t, x^a, p^b)$ ;  $t$  should be thought of as a time-like variable. Since the particles in the ensemble move like test particles, their number density  $f = f(t, x^a, p^b)$  is constant along the geodesics and hence satisfies the Vlasov equation

$$\partial_t f + \frac{p^a}{p^0} \partial_{x^a} f - \frac{1}{p^0} \Gamma_{\beta\gamma}^a p^\beta p^\gamma \partial_{p^a} f = 0. \quad (1.2)$$

The energy-momentum tensor is given by

$$T_{\alpha\beta} = \int p_\alpha p_\beta f |g|^{1/2} \frac{dp^1 dp^2 dp^3}{-p_0}, \quad (1.3)$$

where  $|g|$  denotes the modulus of the determinant of the metric, and indices are raised and lowered using the metric, i.e.,  $p_\alpha = g_{\alpha\beta} p^\beta$ . The system (1.1), (1.2), (1.3) is the Einstein-Vlasov system in general coordinates. We want to

model isolated systems and therefore require that the spacetime is asymptotically flat. In order to simplify the system we only consider spherically symmetric solutions. In the next section we formulate the Einstein-Vlasov system in coordinates adapted to this symmetry. For background on the Einstein-Vlasov system we refer to [1] and the references there.

The Einstein-Vlasov system possesses a plethora of steady state solutions. For a stationary metric the Killing vector  $\partial/\partial t$  gives rise to the quantity  $E = -g(\partial/\partial t, p^\alpha)$  which represents the particle energy and is constant along geodesics. Hence the ansatz

$$f(x^a, p^b) = \phi(E) \tag{1.4}$$

satisfies the stationary Vlasov equation and reduces the system to the field equations. In Section 2.5 we recall how any such “microscopic equation of state  $\phi$ ” gives rise to a one-parameter family of steady states, where the parameter can be identified with the central redshift of the configuration and is therefore a measure of how relativistic it is; the steady states actually considered below can also depend on the angular momentum of the particles. A natural question is which of these steady states are stable or unstable. For the Vlasov-Poisson system, which is the non-relativistic limit of the Einstein-Vlasov system, such steady states essentially are stable if the microscopic equation of state  $\phi$  is a decreasing function of the particle energy, cf. [23] and the references there. For the relativistic case of the Einstein-Vlasov system the situation is quite different. At least on the linearized level it has been shown in [10, 11, 12] that such steady states are stable if their central redshift is sufficiently small, but for the same microscopic equation of state they become unstable if their central redshift is large. The question whether sufficiently relativistic matter distributions become unstable played an important role in the discovery and subsequent discussion of quasars, cf. [7, 15, 30]. But unstable steady states of the Einstein-Vlasov system are also important for conceptual reasons, since they can possibly explain the so-called type I behavior in critical collapse observed for the Einstein-Vlasov system, the latter being related to the cosmic censorship hypothesis, cf. [3, 18, 25]. All this motivates the present investigation where we analyze the transition from stability to instability along one-parameter families of steady states of the Einstein-Vlasov system by numerical means. In particular, we investigate where this transition takes place and what happens to weakly perturbed steady states which lie in the unstable regime.

Concerning the former question there are various possibilities. One can for example consider the so-called binding energy as a function of the central

redshift, cf. Figure 1. It has been conjectured [29, 30] that the transition from stability to instability happens at the first (local) maximum of this curve. For all microscopic equations of state which we consider we confirm this conjecture.

Alternatively, one can plot for a fixed microscopic equation of state and each value of the central redshift the ADM mass and radius of the support of the corresponding steady state. This results in a so-called mass-radius curve, cf. Figure 2. It would be conceivable that the stability properties change at the turning points of this curve since a precise version of this so-called turning point principle has recently been proven both for the Euler-Poisson and the Einstein-Euler system, cf. [9, 16]. In these models, matter is described as an ideal, compressible fluid. The macroscopic quantities induced by an isotropic steady state of the Einstein-Vlasov system of the form (1.4) yield a steady state of the Einstein-Euler system with a suitable, induced macroscopic equation of state, cf. [12]. In particular, the mass-radius curves are then the same for both systems. However, we clearly disprove this turning point principle for the Einstein-Vlasov system.

Another issue is to understand the behavior of solutions which are launched by small perturbations of a stable or an unstable steady state. In the former case we find that the system starts to oscillate, i.e., to expand and contract in a seemingly time-periodic fashion. This behavior was observed in [20] for the Vlasov-Poisson system and in [3] for shell-like solutions of the Einstein-Vlasov system; the code employed in [3] was not able to properly handle steady states which have matter at the center instead of a vacuum region. The behavior of an unstable steady state after perturbation is more interesting. The solution either collapses and forms a black hole, or it seems to follow a heteroclinic orbit to a different, stable steady state about which (the bulk of) it starts to oscillate. The terminology “heteroclinic orbit” may not be quite appropriate here, but it captures the observed behavior. In [28] a similar observation is claimed without further comment. For steady states with a large central redshift the perturbed state may also disperse instead of following a heteroclinic orbit as explained above.

In all the numerical simulations we used dynamically accessible perturbations which in particular preserve all the so-called Casimir functionals (3.1) of the system; perturbing the steady state by some external force results in such dynamically accessible states. All the simulations were performed in three different coordinate systems, namely Schwarzschild, maximal areal, and Eddington-Finkelstein coordinates, and our observations were completely consistent across these. This is a priori not obvious. In a stability analysis for the Einstein-Vlasov system one necessarily must compare func-

tions like metric components or mass-energy densities which are defined on two different spacetimes, the stationary one and the perturbed one. There is no canonical way of identifying points on these two spacetimes so that one could compare the values of certain functions at those identified points. What we do is to simply identify points which have the same coordinates in the coordinate system at hand, and it is therefore not a priori clear that the stability findings in different coordinate systems must be consistent. This point has also been made in the astrophysics literature, cf. [15].

The paper proceeds as follows. In the next section we formulate the Einstein-Vlasov system in the coordinate systems mentioned above, compare these coordinate systems, and recall how steady states of the Einstein-Vlasov system are obtained. In Section 3 we explain the numerical method which we employ, which is a particle-in-cell scheme and lends itself well to parallelization. The numerical results are presented and discussed in Section 4, and in the last section we comment on their precision and reliability.

## 2 The spherically symmetric Einstein-Vlasov system

In this section we formulate the Einstein-Vlasov system in Schwarzschild, maximal areal, and Eddington-Finkelstein coordinates and compare various properties of these coordinate systems. We also recall how steady state solutions can be obtained.

### 2.1 Schwarzschild coordinates

In Schwarzschild coordinates the metric reads

$$ds^2 = -e^{2\mu(t,r)} dt^2 + e^{2\lambda(t,r)} dr^2 + r^2(d\theta^2 + \sin^2\theta d\varphi^2) \quad (2.1)$$

with  $(t, r, \theta, \varphi) \in \mathbb{R} \times [0, \infty[ \times [0, \pi] \times [0, 2\pi]$  and metric coefficients  $\mu = \mu(t, r)$  and  $\lambda = \lambda(t, r)$ . Here,  $t$  corresponds to the proper time of an observer located at spatial infinity and  $r$  denotes the areal radius. For numerical and analytical reasons it is convenient to introduce Cartesian coordinates

$$x = (x^1, x^2, x^3) = r(\sin\theta \cos\varphi, \sin\theta \sin\varphi, \cos\theta) \in \mathbb{R}^3$$

and corresponding non-canonical momentum variables

$$v^i = p^i + \left(e^{2\lambda} - 1\right) \frac{x \cdot p}{r} \frac{x^i}{r}.$$

Since we consider the asymptotically flat case and in order to guarantee a regular center, we impose the boundary conditions

$$\lim_{r \rightarrow \infty} \lambda(t, r) = \lim_{r \rightarrow \infty} \mu(t, r) = \lambda(t, 0) = 0, \quad t \in \mathbb{R}. \quad (2.2)$$

Inserting the metric into the Einstein equations yields the following field equations:

$$e^{-2\lambda}(2r\lambda' - 1) + 1 = 8\pi r^2 \rho, \quad (2.3)$$

$$e^{-2\lambda}(2r\mu' + 1) - 1 = 8\pi r^2 p, \quad (2.4)$$

$$\dot{\lambda} = -4\pi r e^{\mu+\lambda} j. \quad (2.5)$$

These are the 00, 11, and 01 components of the general equation (1.1). Equation (2.5) is not independent, but follows from (2.3) and (2.4) together with the Vlasov equation. However, it is useful for the numerics. The also non-trivial 22 and 33 components of (1.1) follow as well, but they are not used in the numerics. In the above,  $\dot{\phantom{x}}$  and  $'$  denote the derivative with respect to  $t$  or  $r$  respectively. The Vlasov equation takes the form

$$\partial_t f + e^{\mu-\lambda} \frac{v}{\varepsilon} \cdot \partial_x f - \left( \dot{\lambda} \frac{x \cdot v}{r} + \mu' e^{\mu-\lambda} \varepsilon \right) \frac{x}{r} \cdot \partial_v f = 0, \quad (2.6)$$

where we introduce

$$\varepsilon = \sqrt{1 + |v|^2} = \sqrt{1 + w^2 + \frac{L}{r^2}}.$$

Here  $|v|$  denotes the Euclidean length and  $x \cdot v$  the Euclidean scalar product. The variables  $w = \frac{x \cdot v}{r}$  and  $L = |x \times v|^2$  can be thought of as the momentum in the radial direction and the square of the angular momentum respectively. We assume  $f$  to be spherically symmetric, i.e.,  $f(t, x, v) = f(t, Ax, Av)$  for  $A \in \text{SO}(3)$ , and under abuse of notation we may write  $f(t, x, v) = f(t, r, w, L)$ . The source terms in the field equations are defined by

$$\rho(t, r) = \frac{\pi}{r^2} \int_0^\infty \int_{-\infty}^\infty \varepsilon f(t, r, w, L) dw dL, \quad (2.7)$$

$$p(t, r) = \frac{\pi}{r^2} \int_0^\infty \int_{-\infty}^\infty \frac{w^2}{\varepsilon} f(t, r, w, L) dw dL, \quad (2.8)$$

$$j(t, r) = \frac{\pi}{r^2} \int_0^\infty \int_{-\infty}^\infty w f(t, r, w, L) dw dL. \quad (2.9)$$

Here,  $\rho$  is the energy density,  $p$  the radial pressure, and  $j$  the particle current. Equations (2.2)–(2.9) constitute the Einstein-Vlasov system in Schwarzschild coordinates. Unless stated otherwise, we employ the above notation for the other coordinate systems as well.

For later use, we derive some formulas for the metric coefficients. To this end, we introduce the Hawking mass defined as

$$m(t, r) = 4\pi \int_0^r \rho(t, s) s^2 ds. \quad (2.10)$$

Integrating (2.3) yields

$$e^{-2\lambda} = 1 - \frac{2m}{r}; \quad (2.11)$$

the right hand side of this equation remains positive as long as the solution to (2.2)–(2.9) exists. Solving the field equation (2.4) for  $\mu'$  and using (2.11), we obtain

$$\mu' = e^{2\lambda} \left( 4\pi r p + \frac{m}{r^2} \right). \quad (2.12)$$

## 2.2 Maximal areal coordinates

In maximal areal coordinates the line element can be written as

$$ds^2 = (-\alpha^2 + a^2 \beta^2) dt^2 + 2a^2 \beta dt dr + a^2 dr^2 + r^2 (d\theta^2 + \sin^2 \theta d\varphi^2)$$

with positive metric coefficients  $a$  and  $\alpha$ . We note that in the present case  $t$  is not introduced as the proper time of any physical observer, but is fixed by imposing the maximal gauge condition, i.e., each hypersurface of constant  $t$  has vanishing mean curvature. The non-canonical momentum variables introduced in the Schwarzschild case translate to

$$v_i = p_i + \left( \frac{1}{a} - 1 \right) \frac{x \cdot p}{r} \frac{x_i}{r}.$$

In analogy to (2.2) the metric coefficients satisfy the boundary conditions

$$a(t, 0) = \lim_{r \rightarrow \infty} a(t, r) = \lim_{r \rightarrow \infty} \alpha(t, r) = 1, \quad \beta(t, 0) = 0. \quad (2.13)$$

We obtain the field equations

$$\kappa = \frac{\beta}{\alpha r}, \quad (2.14)$$

$$a' = 4\pi r \rho a^3 + \frac{3}{2} r \kappa^2 a^3 + \frac{a}{2r} (1 - a^2), \quad (2.15)$$

$$\kappa' = -3 \frac{\kappa}{r} - 4\pi a j, \quad (2.16)$$

$$\alpha'' = \alpha' \left( \frac{a'}{a} - \frac{2}{r} \right) + 6\alpha a^2 \kappa^2 + 4\pi \alpha a^2 (S + \rho), \quad (2.17)$$

which are coupled to the Vlasov equation

$$\partial_t f + \left[ \frac{\alpha}{a} \frac{v}{\varepsilon} - \beta \frac{x}{r} \right] \cdot \partial_x f + \left[ -\varepsilon \frac{\alpha'}{a} \frac{x}{r} + \alpha \kappa \left( v - 3 \frac{x \cdot v}{r} \frac{x}{r} \right) \right] \cdot \partial_v f = 0 \quad (2.18)$$

via the source terms (2.7), (2.9), and

$$S(t, r) = \frac{\pi}{r^2} \int_0^\infty \int_{-\infty}^\infty \frac{\varepsilon^2 - 1}{\varepsilon} f(t, r, w, L) dw dL, \quad (2.19)$$

the trace of the spatial part of the energy-momentum tensor.

As in Schwarzschild coordinates we introduce the Hawking mass, which in maximal areal coordinates becomes

$$m = \frac{r}{2} \left( 1 - \frac{1}{a^2} + r^2 \kappa^2 \right).$$

In order to solve the field equations numerically, it is useful to consider the quantity

$$\eta = \frac{r}{2} \left( 1 - \frac{1}{a^2} \right),$$

which immediately implies

$$\eta(t, r) = \int_0^r \left( 4\pi \rho(t, s) + \frac{3}{2} \kappa^2(t, s) \right) s^2 ds. \quad (2.20)$$

Furthermore, the field equation (2.16) yields the implicit formula

$$\kappa(t, r) = -\frac{4\pi}{r^3} \int_0^r a(t, s) j(t, s) s^3 ds,$$

while

$$\alpha'(t, r) = \frac{a(t, r)}{r^2} \int_0^r (4\pi a \alpha (\rho + S) + 6\alpha \kappa^2) s^2 ds$$

holds because of the second order equation (2.17). Note that  $\kappa(t, r) \sim r^{-3}$  for large  $r$  provided that the matter is compactly supported.



### 2.3 Eddington-Finkelstein coordinates

In Eddington-Finkelstein coordinates the metric takes the form

$$ds^2 = -a(t, r)b^2(t, r)dt^2 + 2b(t, r)dt dr + r^2(d\theta^2 + \sin^2\theta d\varphi^2).$$

Similar to (2.2) and (2.13) the metric coefficients  $a$  and  $b$  satisfy the boundary conditions

$$a(t, 0) = \lim_{r \rightarrow \infty} a(t, r) = \lim_{r \rightarrow \infty} b(t, r) = 1. \quad (2.21)$$

Notice that the metric coefficient  $a$  here is not the same as the coefficient  $a$  appearing in maximal areal coordinates, but we nevertheless use this quite common, albeit equivocal notation. As opposed to Schwarzschild and maximal areal coordinates we use the canonical momentum coordinates  $(p_0, p_1, p_2, p_3)$ . The angular momentum is given by

$$L = (p_2)^2 + \frac{1}{\sin^2\theta}(p_3)^2.$$

The particle density  $f$  can be written as a function of  $(t, r, p_1, L)$  and the Vlasov equation reads

$$\begin{aligned} \partial_t f + \frac{b}{2} \left( a - \frac{1 + L/r^2}{(p_1)^2} \right) \partial_r f \\ + \frac{1}{2} \left( \frac{2bL}{r^3 p_1} - \partial_r(ab)p_1 - \partial_r b \frac{1 + L/r^2}{p_1} \right) \partial_{p_1} f = 0. \end{aligned}$$

Here, the Hawking mass  $m$  is given by

$$m = \frac{r}{2}(1 - a).$$

The metric coefficients  $a$  and  $b$  as well as the Hawking mass can be computed directly from  $f$  via

$$\begin{aligned} b(t, r) &= \exp \left( -4\pi \int_r^\infty \eta T_{11}(t, \eta) d\eta \right), \\ m(t, r) &= \frac{2\pi}{b(t, r)} \int_0^r \eta^2 (T_{11} + S)(t, \eta) b(t, \eta) d\eta, \\ a(t, r) &= 1 - \frac{2m(t, r)}{r}, \end{aligned}$$

where

$$T_{11}(t, r) = \frac{\pi}{r^2} \int_0^\infty \int_0^\infty p_1 f(t, r, p_1, L) dL dp_1,$$

$$S(t, r) = \frac{\pi}{r^2} \int_0^\infty \int_0^\infty \frac{1 + \frac{L}{r^2}}{p_1} f(t, r, p_1, L) dL dp_1.$$

We have to keep in mind that the physical interpretation of the timelike variable  $t$  differs across the three coordinate systems, and we should mention that in Eddington-Finkelstein coordinates, what we called  $t$  is usually denoted as  $v$ .

## 2.4 Properties and comparison of the coordinate systems

Before we investigate the system numerically, we briefly discuss and compare selected properties of the coordinate systems. Two conserved quantities of the system are the total number of particles or total rest mass and the ADM mass. Across all coordinate systems the latter is given by

$$M = \lim_{r \rightarrow \infty} m(t, r). \quad (2.22)$$

For compactly supported matter this equals the Hawking mass evaluated at the outer boundary of the radial support.

The total number of particles is computed differently across the coordinate systems. In the Schwarzschild case we have

$$N = 4\pi^2 \int_0^\infty \int_{-\infty}^\infty \int_0^\infty e^{\lambda(t, r)} f(t, r, w, L) dr dw dL, \quad (2.23)$$

while in maximal areal coordinates,

$$N = 4\pi^2 \int_0^\infty \int_{-\infty}^\infty \int_0^\infty a(t, r) f(t, r, w, L) dr dw dL, \quad (2.24)$$

and in Eddington-Finkelstein coordinates,

$$N = 4\pi^2 \int_0^\infty \int_0^\infty \int_0^\infty f(t, r, p_1, L) dr dp_1 dL. \quad (2.25)$$

The weights  $e^\lambda$  and  $a$  appear because the characteristic flow is not measure preserving. This is due to the use of non-canonical momentum variables. In fact, if by  $D$  we denote differentiation along a characteristic of the Vlasov equation, then in the Schwarzschild case

$$D(f dx dv) = -\left(\dot{\lambda} + \lambda' e^{\mu-\lambda} \frac{w}{\varepsilon}\right) f dx dv$$

and in the maximal areal case

$$D(f \, dx \, dv) = - \left( \frac{\alpha a'}{a^2} \frac{w}{\varepsilon} + \beta' + \frac{2\beta}{r} \right) f \, dx \, dv.$$

In Eddington-Finkelstein coordinates canonical momentum variables are used which implies  $D(f \, dx \, dv) = 0$ .

Another important difference between the three coordinate systems is the existence of a criterion for the formation of trapped surfaces. There exists no such criterion in Schwarzschild coordinates since these coordinates cannot cover an open region which contains a trapped surface. In maximal areal coordinates a trapped surface is present when

$$\frac{1}{a(t, r)} - r\kappa(t, r) < 0. \quad (2.26)$$

In this case, the expansion of both outgoing and ingoing null geodesics is negative at the time  $t$  on the sphere of radius  $r$ . This signals the development of a spacetime singularity, cf. [19]. In Eddington-Finkelstein coordinates the condition

$$a(t, r) < 0 \quad (2.27)$$

corresponds to the existence of a trapped surface, cf. [6].

In Schwarzschild coordinates there exists a local existence and uniqueness result for smooth, compactly supported initial data together with a continuation criterion for such solutions, cf. [22, 24]. An analogous result holds in maximal areal coordinates, cf. [8], but probably not in Eddington-Finkelstein coordinates, at least not for general smooth data whose support contains the origin. In general, Schwarzschild or maximal areal coordinates are more useful when proving that certain data launch global, geodesically complete solutions, cf. [2, 24], while the formation of trapped surfaces for suitable data has been shown in Eddington-Finkelstein coordinates, cf. [6]. The stability analysis in [10, 11, 12] was carried out in Schwarzschild coordinates.

## 2.5 Steady state solutions

Despite the differences of the above coordinate systems, there exists an explicit coordinate transformation which maps stationary solutions in one coordinate system into stationary solutions in the other two. For this reason we discuss steady states in Schwarzschild coordinates first.

A simple calculation shows that for a time-independent metric the particle energy

$$E = \begin{cases} \varepsilon e^\mu & \text{for Schwarzschild,} \\ \varepsilon \alpha & \text{for maximal areal,} \\ \frac{b}{2} \left( ap_1 + \frac{1+L/r^2}{p_1} \right) & \text{for Eddington-Finkelstein} \end{cases}$$

is conserved along characteristics of the Vlasov equation, and due to spherical symmetry the same is true for the square of the angular momentum  $L$ . Thus, every ansatz of the form  $f_0 = \phi(E, L)$  solves the Vlasov equation in the time-independent metric and reduces the system to the field equations for that metric, where the source terms now depend on the latter through the given ansatz. In the present paper we consider two different types of ansatz functions, namely the polytropic ansatz

$$f_0 = \left( 1 - \frac{E}{E_0} \right)_+^k (L - L_0)_+^l \quad (2.28)$$

and the King model

$$f_0 = \left( e^{1 - \frac{E}{E_0}} - 1 \right)_+. \quad (2.29)$$

Here  $z_+$  denotes the positive part of some number  $z$ . The constants  $E_0 > 0$  and  $L_0 \geq 0$  are the cut-off energy and the minimal angular momentum while  $k \geq 0$  and  $l \geq 0$  are prescribed parameters. In order to guarantee the existence of stationary solutions with finite ADM mass and compact support [20], we choose  $k < l + \frac{3}{2}$ , but also consider the borderline case of  $k = \frac{3}{2}$  and  $l = 0$ . The cut-off energy is necessary to ensure finite extension and finite ADM mass of the corresponding stationary solution. Prescribing  $L_0 > 0$  gives rise to a vacuum region at the center and hence to a shell type solution. On the other hand, choosing  $L_0 = 0$  implies that the support of the steady state contains the origin. Note that the factor  $(L - L_0)_+^l$  can also be multiplied to the King ansatz, with the analogous effect on the support of the resulting steady state.

Even though multiple radially separated shells may arise from a polytropic ansatz with  $L_0 > 0$ , we only consider the innermost shell as our steady state, cf. [4]. Formally, these steady states depend not only on  $E$  and  $L$  but also on the choice of the shell. However, we still refer to them as polytropes.

In order to solve for the metric coefficients, it turns out to be more convenient to consider  $y = \ln E_0 - \mu$ . For an ansatz as above we can write

the spatial mass density and pressure as functions of  $y$ , i.e.,

$$\rho(r) = g(y(r)), \quad p(r) = h(y(r)).$$

For the definition of  $g$  and  $h$  and further details we refer to [20]. The stationary Einstein-Vlasov system is then reduced to the differential equation

$$y' = -\frac{1}{1 - \frac{8\pi}{r} \int_0^r g(y(s)) s^2 ds} \left( \frac{4\pi}{r^2} \int_0^r g(y(s)) s^2 ds + 4\pi r h(y(r)) \right). \quad (2.30)$$

This equation is (2.12) with (2.11) substituted in. For every choice of  $y(0) = y_0 > 0$ , [20] guarantees a unique solution of (2.30) with finite ADM mass and compact support. Hence one given ansatz of the form (2.28) or (2.29) yields a one-parameter family of such steady states. The parameter is closely connected to the central redshift  $z_c$ , measuring the redshift of a photon which is emitted at the center  $r = 0$  and received at the boundary of the steady state:

$$z_c = e^{y_0} - 1. \quad (2.31)$$

This is not the standard definition of the central redshift where the photon is received at infinity, but our definition is more suitable here. If  $y$  is a solution to (2.30) and the cut-off energy is defined as  $E_0 = \lim_{r \rightarrow \infty} e^{y(r)}$ , the metric coefficient  $\mu = \ln E_0 - y$  satisfies the proper boundary condition at infinity, and  $\lambda$  is given by

$$\lambda(r) = -\frac{1}{2} \ln \left( 1 - \frac{8\pi}{r} \int_0^r \rho(s) s^2 ds \right).$$

We now discuss how to obtain the stationary solutions in the other two coordinate systems. In maximal areal coordinates stationary solutions satisfy  $\kappa = \beta = j = 0$ . The metric is then equivalent to the Schwarzschild metric by simply setting  $\mu = \ln \alpha$  and  $\lambda = \ln a$ , cf. [3]. In the case of Eddington-Finkelstein coordinates the metric coefficients  $a$  and  $b$  can be obtained by the change of variables

$$t \mapsto t + \int_0^r e^{\lambda(s) - \mu(s)} ds,$$

and the metric coefficients are related via

$$a = e^{-2\lambda}, \quad b = e^{\lambda + \mu}.$$

Before we discuss how we solve the time-dependent Einstein-Vlasov system, we briefly explain how we compute the steady states. For a prescribed ansatz function of the form (2.28) or (2.29) as well as  $y_0 > 0$ , we compute the corresponding solution  $y$  to the equation (2.30). We use the explicit Euler method enhanced with a leap frog scheme to solve (2.30) and apply Simpson's rule to calculate the integrals appearing in  $g$ ,  $h$ , and (2.30). Note that the whole steady state computation has to be done only once, which allows us to use very high accuracy for this part. The distribution function  $f_0$  of the steady state is then given via (2.28) or (2.29).

### 3 The numerical method for the time evolution

The algorithms used to investigate the stability of steady states of the above system are based on the particle-in-cell scheme. This scheme has also been used in [3, 21, 25]. For the spherically symmetric Vlasov-Poisson system its convergence has been shown in [27], the analogous result for the Einstein-Vlasov system in Schwarzschild coordinates is shown in [26]. In a particle-in-cell scheme the support of the distribution function  $f$  is initially split into distinct cells. Into each cell a numerical particle is placed to represent the contribution to  $f$  of this cell, and these particles are then propagated according to the Einstein-Vlasov system. Most of the following steps differ for the three coordinate systems under investigation. We focus on the algorithm for Schwarzschild coordinates, but always highlight difficulties arising in the other two coordinate systems and how to overcome them.

To initialize the numerical particles we use variables adapted to the spherical symmetry of the steady state  $f_0$ , i.e., we write

$$f_0 = f_0(r, w, L) = f_0(r, u, \psi),$$

where we use the additional variables  $u \geq 0$  and  $\psi \in [0, \pi]$  given by

$$u^2 = w^2 + \frac{L}{r^2}, \quad w = u \cos(\psi).$$

Assuming that  $f_0$  vanishes outside of the set  $[R_-, R_+] \times [U_-, U_+] \times [\Psi_-, \Psi_+]$ , we prescribe a radial step length  $\Delta r > 0$  as well as integers  $N_u$  and  $N_\psi$  to define the step lengths

$$\Delta u = \frac{U_+ - U_-}{N_u}, \quad \Delta \psi = \frac{\Psi_+ - \Psi_-}{N_\psi}$$

and set up a grid of points

$$r_i = \left(i - \frac{1}{2}\right)\Delta r, \quad u_j = \left(j - \frac{1}{2}\right)\Delta u, \quad \psi_k = \left(k - \frac{1}{2}\right)\Delta\psi.$$

At each point  $(r_i, u_j, \psi_k)$  we generate a numerical particle carrying the weight

$$f_{i,j,k} = f_0(r_i, u_j, \psi_k) 4\pi r_i^2 \Delta r 2\pi u_j^2 \Delta u \sin(\psi_k) \Delta\psi,$$

where  $f_0(r_i, u_j, \psi_k)$  is calculated using the steady state from above. We use  $(r, u, \psi)$ -variables in Schwarzschild and maximal areal coordinates to generate the numerical particles. In the Eddington-Finkelstein case a similar initialization scheme based on  $(r, p_1, L)$ -variables is used. For the following steps it is convenient for Schwarzschild and maximal areal coordinates to write the particle positions in  $(r, w, L)$ -variables, since  $L$  is conserved along characteristics.

We then compute the matter quantities  $\rho$ ,  $p$ , and  $j$  on the fixed radial grid given by  $r_j = j\Delta r$  by integrating  $f_0$  according to (2.7), (2.8), and (2.9). This is implemented by adding up  $f_{i,j,k}$  with the appropriate weight given by (2.7)-(2.9) and by a linear interpolation of  $f_0$  in the radial direction; note that  $f_{i,j,k}$  contains the phase space volume element.

Next, we compute the Hawking mass  $m$  on the fixed radial grid by using (2.10) and a quadratic interpolation, taking into account the possible order of the integrand near the origin. Afterwards, the metric quantity  $\mu$  is calculated by applying (2.11), (2.12), and the boundary condition  $\mu(R) = \lambda(R)$ , where  $R$  denotes the outer boundary of the radial support.

In maximal areal coordinates we instead solve for  $\eta$  and  $\kappa$  simultaneously by employing a fourth-order Runge-Kutta method in order to guarantee sufficient numerical precision and to appropriately handle the implicit structure of the field equations. Determining  $\alpha$  requires more effort due to the ellipticity of equation (2.17) and the boundary condition given at spatial infinity. We choose a sufficiently large grid, approximate the various derivatives and arrive at a tridiagonal system which can be solved explicitly. For more details consider the scheme used in [3].

The time step is then performed by propagating the numerical particles according to the characteristic system corresponding to the Vlasov equation. In order to avoid numerical errors at the spatial origin caused particularly by particles coming close to the origin, it is advantageous to use Cartesian coordinates for the propagation. Here, all functions involved are interpolated according to their order, especially near the origin. However, we do not use

Cartesian coordinates in the case of Eddington-Finkelstein coordinates since the metric written in these coordinates is not continuous at the origin, cf. [6]. The new position of each particle is then computed by a proper stepping method with a prescribed time step size  $\Delta t > 0$ . Note that we also have to update the weight  $f_{i,j,k}$  during each time step in the case of Schwarzschild and maximal areal coordinates, since the characteristic flow of the Vlasov equation system is not measure preserving in these coordinates.

At this point the particle coordinates and weights are known at the time  $\Delta t$  and we can repeat the iteration until we reach some final time  $T$  which is prescribed from the beginning.

So far we have numerically evolved a steady state  $f_0$  itself, but in order to analyze its stability properties we have to perturb it. In [3] this is done by taking  $A f_0$  for some parameter  $A \approx 1$  as an initial condition. However, this kind of perturbation is not natural from a physics point of view since it is not dynamically accessible, i.e., it does not preserve Casimir functionals of the form

$$\mathcal{C}(f(t)) = \iint e^{\lambda(t,x)} \chi(f(t,x,v)) dx dv \quad (3.1)$$

where  $\chi \in C^1(\mathbb{R})$  with  $\chi(0) = 0$ ; a physically viable perturbation for example by some external force should preserve these. We provide a perturbation procedure preserving these invariants. An analogous type of perturbation has been used in [21] for the Vlasov-Poisson system, but as far as we know this is the first implementation of dynamically accessible perturbations to steady states of the Einstein-Vlasov system. During an initial time interval  $[0, T_{pert}]$  we propagate the numerical particles according to the modified characteristic system

$$\dot{x} = e^{\mu-\lambda} \frac{v}{\varepsilon}, \quad \dot{v} = -\left(\dot{\lambda} \frac{x \cdot v}{r} + \mu' e^{\mu-\lambda} \varepsilon\right) \frac{x}{r} + \gamma \frac{x}{r} \quad (3.2)$$

in the Schwarzschild case for prescribed  $\gamma \approx 0$ . Compared to the original characteristic system, we add the term  $\gamma \frac{x}{r}$  to the right hand side of the equation for  $\dot{v}$ . Since Casimir functionals are preserved along solutions of the Vlasov equation and the above perturbation does not contribute to the divergence of the right hand side of the characteristic system, this perturbation is indeed dynamically accessible. In maximal areal coordinates we also add the divergence free term  $(0, \gamma \frac{x}{r})$  to the right hand side of the respective characteristic system during an initial time interval. In Eddington-Finkelstein coordinates, where  $E = E(r, p_1)$  is the Hamiltonian governing the motion of the particles, we add  $\gamma r p_1$  as a perturbation of the Hamiltonian.



Despite the fact that  $v$  does not denote the canonical momentum, all these perturbations can be interpreted as particles being accelerated either radially outwards if  $\gamma > 0$  or radially inwards if  $\gamma < 0$ .

We refer to the evolved state at  $t = T_{pert}$  as the perturbed state. To determine the intensity of the perturbation we consider  $e^{\mu(t,0)}$ ,  $\alpha(t,0)$ , and  $b(t,0)$  respectively. We prescribe a small number  $\epsilon_{pert}$  and then choose  $\gamma$  such that the relative error of  $e^{\mu(t,0)}$  between  $t = 0$  and  $t = T_{pert}$  is close to  $\epsilon_{pert}$ . Obviously, numerical and evolutionary effects contribute to the perturbation of the steady state as well. To this end, we choose  $\epsilon_{pert}$  such that it dominates the relative error of the above quantities resulting from the numerical initialization. In addition, we choose  $T_{pert}$  sufficiently small such that evolutionary effects are negligible.

We emphasize that we have tested several other perturbations. On the one hand, we used rather simple perturbations where we scale the steady state by some factor or shift it slightly in one direction. On the other hand, we employed further dynamically accessible perturbations where we propagate the numerical particles using modified metric quantities during an initial time interval. For every kind of perturbation there seem to exist precisely two distinct characteristic behaviors: pushing the steady state either towards collapse or towards dispersion. However, all the effects described in the next section seem to only depend on the direction of the perturbation but not on its specific type.

Let us end this section with a remark concerning the numerical implementation. In order to obtain reliable physical results, we have to work with tens of millions of numerical particles and sufficiently small time steps. For these simulations to run within a reasonable time-frame, the programs have to be parallelized, which however fits very well with the particle-in-cell scheme. We refer to [17] for a detailed discussion.

## 4 Results

In the following we investigate the stability behavior of the one-parameter families of steady states which we obtain by choosing the King model or the polytropic ansatz with fixed parameters  $k$ ,  $l$ , and  $L_0$ . Due to its physical relevance we mainly present the results for the King model. The parameter that determines the steady state is the central value  $y_0$  where larger values of  $y_0$  generally indicate more relativistic scenarios, cf. (2.31). For a detailed overview of properties of the steady states we refer to [4].

A physically meaningful quantity of a steady state is its binding energy

$$E_b = \frac{N - M}{N},$$

where  $N$  is the number of particles and  $M$  the ADM mass. In Figure 1 the binding energy is plotted against  $y_0$  for different models, namely for the King model and polytropes with  $(k, l, L_0) = (0.5, 0, 0)$ ,  $(0.5, 0, 0.001)$ ,  $(0.5, 0.1, 0.001)$ . We observe that the binding energy has the same qualitative features across the different models: It develops a positive local maximum after which it drops below zero. Despite the fact that the parameter

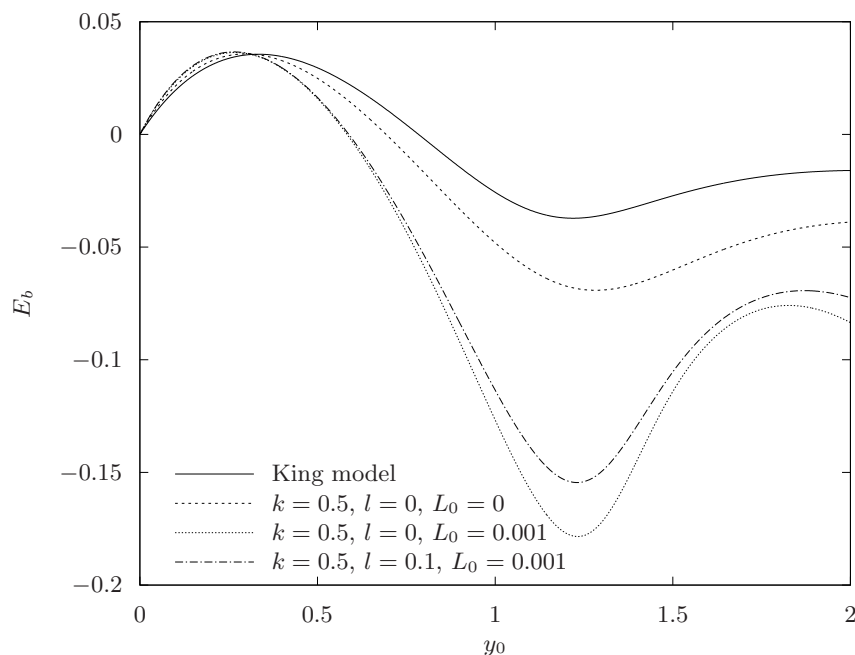


Figure 1: Binding energy for different models.

$L_0 = 0.001$  may seem very small, it still suffices to change the corresponding one-parameter family of steady states significantly. Table 1 gives the values  $y_{\max}$  and  $y_{\text{zero}}$  where the binding energy attains its first maximum or its first zero respectively for the different models used in Figure 1. Another way to visualize a one-parameter family of steady states originating from a given ansatz function is the so-called mass-radius diagram where for each value of  $y_0 > 0$  one plots the ADM mass and radius of the corresponding steady state. In Figure 2 this is done for the King model.

| Model                           | $y_{\max}$ | $y_{\text{zero}}$ |
|---------------------------------|------------|-------------------|
| King                            | 0.334      | 0.784             |
| $k = 0.5, l = 0, L_0 = 0$       | 0.298      | 0.693             |
| $k = 0.5, l = 0, L_0 = 0.001$   | 0.267      | 0.583             |
| $k = 0.5, l = 0.1, L_0 = 0.001$ | 0.265      | 0.588             |

Table 1: First binding energy maximizer and zero.

The spiral structure is a general feature of these mass-radius diagrams for the Einstein-Vlasov system, cf. [4]. According to the so-called turning point principle the steady state should pass from being stable to being unstable as it crosses the first maximum point along the curve, but we find that this is not true.

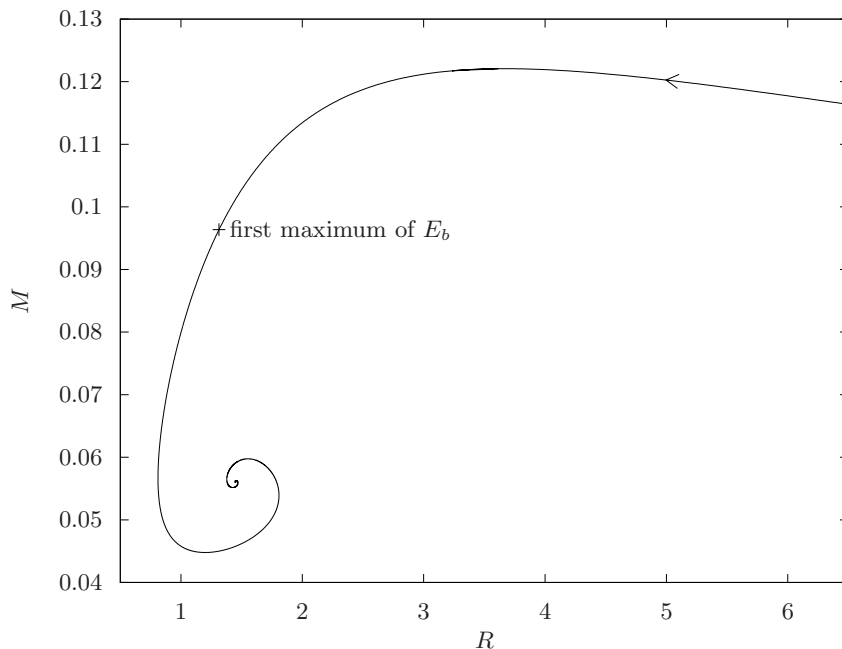


Figure 2: Mass-radius spiral for the King model; as  $y_0$  increases the corresponding  $(R, M)$  moves into the spiral.

As mentioned at the end of Section 3, perturbations can be categorized as either promoting collapse or promoting dispersion. For example, the dynamically accessible perturbation of  $f_0$  with parameter  $\gamma$  described in (3.2)

pushes the steady state towards collapse if  $\gamma < 0$ , and towards dispersion if  $\gamma > 0$ .

#### 4.1 Stable steady states

For small values of  $y_0$  we find that the steady states are stable with respect to every reasonable perturbation. However, perturbations do not leave the steady state unchanged but make it oscillate in a pulsating manner. Similar oscillations have been numerically observed as perturbations of stable steady states of the Vlasov-Poisson system, cf. [21]. Figure 3 illustrates this behavior on the level of the mass distribution. Alternatively, the quantity

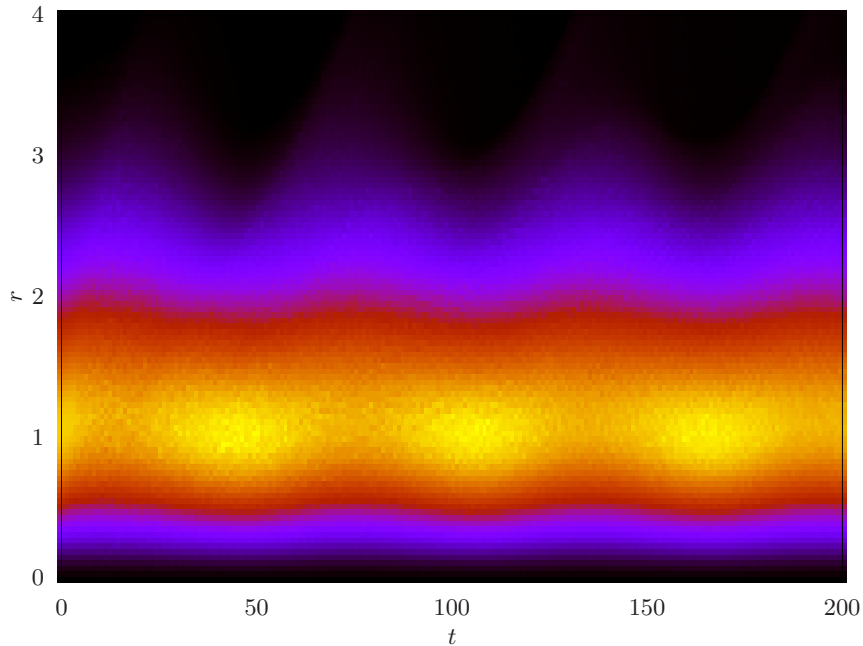


Figure 3: The oscillation of the weighted mass density  $4\pi r^2 \rho$  for the King model in Schwarzschild coordinates for  $y_0 = 0.1$  perturbed by a dynamically accessible perturbation with direction  $\gamma > 0$ . The color represents the value of  $4\pi r^2 \rho$ , increasing from black to yellow.

$e^{\mu(t,0)}$ ,  $\alpha(t,0)$ , or  $b(t,0)$ , respectively, is a good indicator of an oscillation—or other solution behaviors—since it is the relativistic counterpart of the gravitational potential at the spatial origin. In addition, these quantities are integrated from infinity inwards which makes them less volatile from a numerical point of view while they are influenced by the solution as a whole.

For a comparison of the effect of different signs of  $\gamma$  when perturbing a stable steady state consider Figure 4. On the one hand, for a perturbation

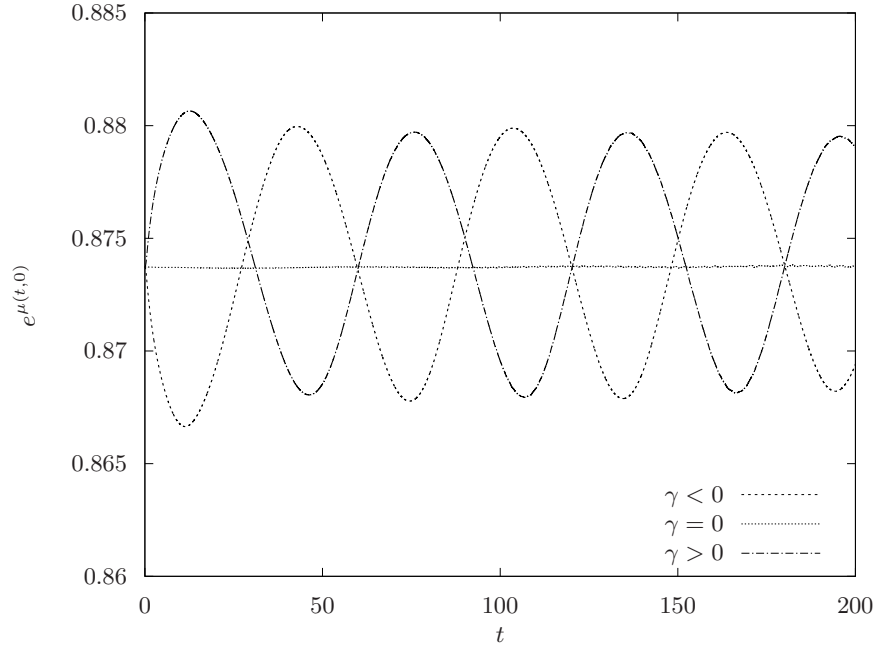


Figure 4: The King model in Schwarzschild coordinates for  $y_0 = 0.1$  perturbed by dynamically accessible perturbations with directions  $\gamma < 0$ ,  $\gamma = 0$ , and  $\gamma > 0$ .

that promotes collapse ( $\gamma < 0$ ) the quantity  $e^{\mu(t,0)}$  initially decreases. On the other hand,  $e^{\mu(t,0)}$  initially increases for a perturbation that promotes dispersion ( $\gamma > 0$ ). In both cases an oscillation of the perturbed steady state develops. Concerning the period of such oscillations, we observe that it depends on the specific steady state model as well as the strength of the perturbation itself. The period seems to approach a fixed positive value as the strength of the perturbation is gradually decreased, but in the context of stability issues it is not relevant to determine the periods of perturbed stable steady states.

Across all models and coordinate systems, we observe that the steady states are stable for small values of  $y_0$ . At some threshold value the stability behavior changes.

## 4.2 The first binding energy maximum—onset of instability

One main goal of our numerical investigation of the time dependent system is to detect when instability of steady states first occurs along a one-parameter family. We find convincing evidence that the so-called “binding energy maximum hypothesis” holds which has also been analyzed and confirmed in [3, 13, 14, 28] for different models and perturbations. It was first proposed by Zel’dovich et al. in [29, 30]. The hypothesis states that the first binding energy maximum along a steady state sequence signals the onset of instability.

The starting point of our investigation is [3] where the binding energy maximum hypothesis has been verified numerically in maximal areal coordinates for the case of polytropic shell steady states, i.e.,  $L_0 > 0$  in (2.28). We are able to confirm the findings of [3] in all three coordinate systems. Furthermore, we expand these results to polytropes with no inner vacuum region, i.e.,  $L_0 = 0$ , and in particular to isotropic models, i.e.,  $L_0 = 0$  and  $l = 0$ , which allows particles to pass through the origin. Our findings clearly support the binding energy maximum hypothesis in these cases.

We present the results of simulations for four cases across the three coordinates systems: the isotropic case for  $k = 0.5, 1, 1.5$  and the King model. In every case we determine the first maximizer of the binding energy, defined as  $y_{\max}$ , with sufficient accuracy. We then consider steady states with values of  $y_0$  close to  $y_{\max}$ . As mentioned in Section 4.1 we find that the steady states are stable for both types of perturbations for  $y_0 < y_{\max}$  across all models and coordinate systems. For  $y_0 > y_{\max}$  the stability behavior changes. In fact, in all coordinate systems and models we observe that a perturbation promoting collapse leads to the actual collapse of the steady state to a black hole, which is illustrated in Figure 5. Notice that for  $y_0 < y_{\max}$  we observe periodic oscillations even when  $y_0$  is very close to  $y_{\max}$ . We elaborate on the details of a collapse in the next section.

Perturbations promoting dispersion neither lead to collapse nor full dispersion but invoke an oscillation of the system. This may lead one to believe that the steady states for  $y_0 > y_{\max}$  are in fact stable with respect to the dispersive perturbation. However, by taking a closer look at  $e^{\mu(t,0)}$  in these cases, we notice that the oscillating quantity seems to drift upwards which contradicts the perception of stability, i.e., an oscillation around the original steady state. This behavior is shown in Figure 6. The attentive reader will have noticed that in Figure 6 the aforementioned drift seems to appear for  $y_0 < y_{\max}$  close to  $y_{\max}$  as well. However, further simulations showed that the latter drift is an artifact of mere numerical inaccuracy. For example,

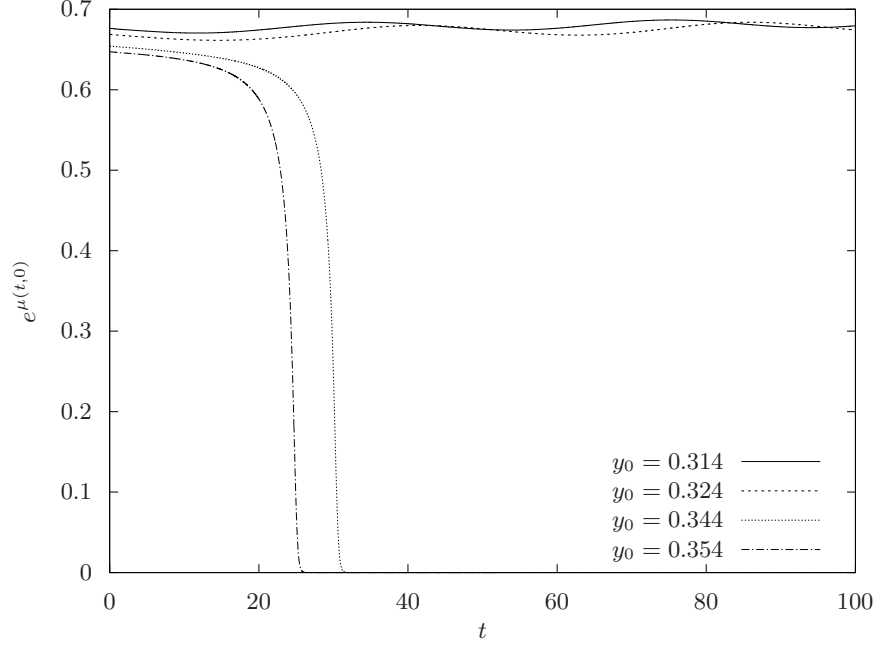


Figure 5: The King model in Schwarzschild coordinates for  $y_0$  close to  $y_{\max}$  perturbed by a dynamically accessible perturbation with direction  $\gamma < 0$ .

the drift weakens when decreasing the time increment  $\Delta t$ . This might be an effect related to the well-known energy drift for Hamiltonian systems.

The crucial observation is that for  $y_0 > y_{\max}$  the initial elevation of  $e^{\mu(t,0)}$  significantly differs from the initial behavior for  $y_0 < y_{\max}$ . On the one hand, for  $y_0 = 0.314$  and  $y_0 = 0.324$  in Figure 6, i.e.,  $y < y_{\max}$ , the oscillation starts immediately and the first local maximum is at about  $t = 15$ . On the other hand, for  $y_0 = 0.344$  and  $y_0 = 0.354$  there exists an initial phase over the course of which the increase of  $e^{\mu(t,0)}$  seems to occur independently from the oscillation. Therefore, the first local maximum appears much later at about  $t = 50$ . The general behavior for  $y_0 > y_{\max}$  will be analyzed more closely in Section 4.4.

We now come back to the question whether the turning point principle is valid for the Einstein-Vlasov system. As explained above, our numerics show that in a one-parameter family steady states are stable as long as  $y_0 < y_{\max}$ , and they become unstable as soon as  $y_0 > y_{\max}$ ; the change from stability to instability occurs at the first maximum of the binding energy. In the mass-radius spiral in Figure 2 we have marked the point which corresponds

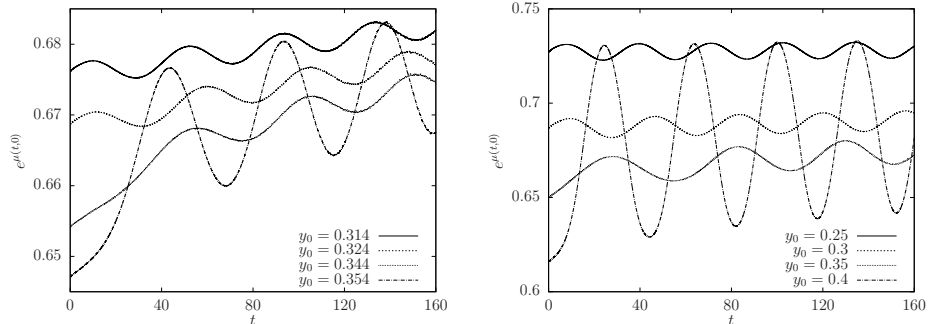


Figure 6: The King model in Schwarzschild coordinates for  $y_0$  close to  $y_{\max}$  perturbed by a dynamically accessible perturbation with direction  $\gamma > 0$ . Notice the different scales.

to  $y_{\max}$ , i.e., to the first maximum of the binding energy. But this point is clearly to the left of the first turning point of the mass-radius spiral, i.e., steady states for the Einstein-Vlasov system remain stable even after the turning point principle would predict their instability and after the very same steady states have become unstable as steady states of the Einstein-Euler system. We have observed this discrepancy or failure of the turning point principle in all cases which we investigated numerically, and it seems a very interesting mathematical problem to properly understand this issue.

### 4.3 Properties of the collapse

One of the main advantages of using three coordinate systems is the possibility to observe the properties of collapsing matter from different perspectives. In Schwarzschild coordinates we have no analytical criterion for the detection of a trapped surface. However, the ratio  $\frac{2m(t,r)}{r}$  approaching 1 at some radius signals the development of a black hole. On the contrary, in maximal areal and Eddington-Finkelstein coordinates trapped surfaces can be detected analytically, cf. (2.26) and (2.27). Note that rapidly increasing metric coefficients eventually cause the program to break down in the event of a collapse.

First, let us explain our observations when a collapse to a black hole occurs. As far as the numerical particles within the simulation are concerned, we notice that the matter focuses towards the origin and the matter density  $\rho$  increases at the center. In fact, in our simulations no particles remain unaffected by the collapse, and all particles are eventually and irreversibly sucked towards the interior of the trapped surface. This eventually leads to the ra-



dius  $R$  of the support of the solution tending to the Schwarzschild radius  $2M$ . This general behavior should be compared to the analytical findings in [5]. The observations on the particle level can be linked to the characteristic behavior of metric coefficients. In Schwarzschild and maximal areal coordinates the collapse is reflected in the behavior of the functions  $e^\mu$  and  $\alpha$ , respectively. These quantities rapidly decrease to zero in close proximity of the origin while still satisfying the boundary conditions at infinity, cf. (2.2) and (2.13). In the literature, this phenomenon is commonly known as the “collapse of the lapse” since  $e^\mu$  and  $\alpha$  determine the amount of proper time which elapses from one hypersurface of constant  $t$  to the next. The collapse of the lapse is depicted in Figure 7 where we can see an exponential decay of  $\alpha$  for late times and  $r$  close to zero. In Eddington-Finkelstein coordinates, the metric coefficient  $b$  shows a similar behavior. Furthermore, the criteria

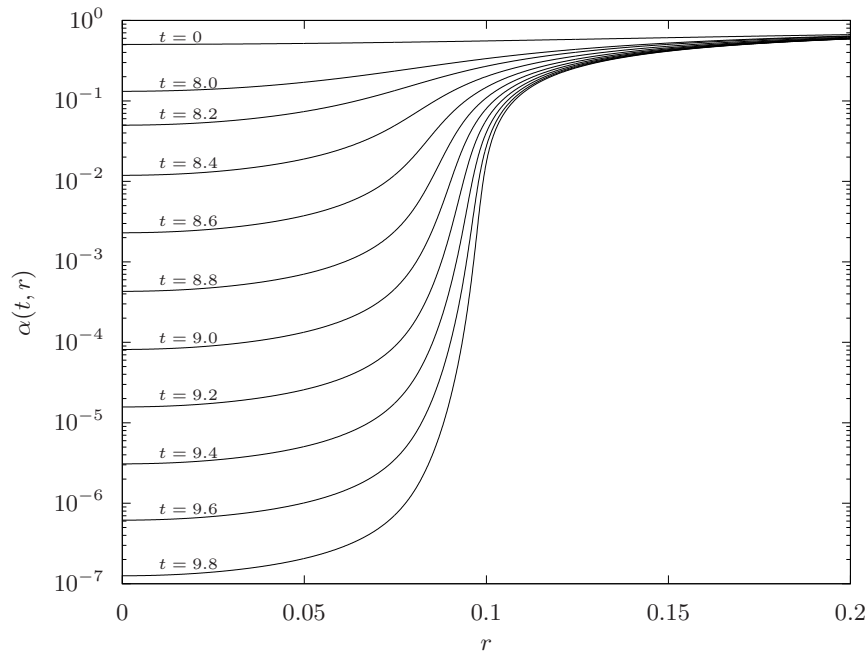


Figure 7: Evolution of  $\alpha(t, r)$  for the King model in maximal areal coordinates for  $y_0 = 0.6$  perturbed by a dynamically accessible perturbation with direction  $\gamma < 0$ . Notice the logarithmic scale.

for the formation of a trapped surface mentioned above are satisfied from some moment in time onwards. Figure 8 shows the evolution of the metric coefficient  $a$  in Eddington-Finkelstein coordinates where  $a < 0$  corresponds

to the occurrence of a trapped surface, cf. Section 2.4. In particular, the radius at which the first trapped surface forms is significantly larger than the chosen radial increment  $\Delta r$ . This supports the conjecture that the weak censorship hypothesis holds for the Einstein-Vlasov system in our setting. For an overview of this topic we refer to [1]. Independently of the choice

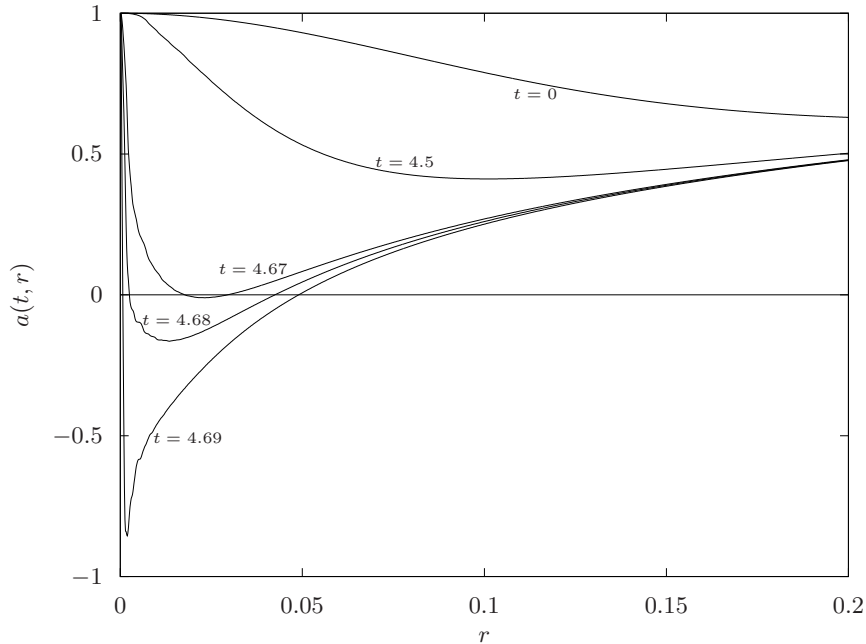


Figure 8: Evolution of  $a(t, r)$  for the King model in Eddington-Finkelstein coordinates for  $y_0 = 0.6$  perturbed by a dynamically accessible perturbation with direction  $\gamma < 0$ .

of the coordinate system, we observe that the coordinate time it takes until an unstable steady state collapses decreases as  $y_0$  is enlarged. This can be explained by the fact that larger values of  $y_0$  correspond to more relativistic steady states. However, one should recall that the time coordinate  $t$  has a different meaning across the three coordinate systems.

#### 4.4 Heteroclinic orbits

When perturbing an unstable steady state with a perturbation promoting dispersion, i.e.,  $y_0 > y_{\max}$  and  $\gamma > 0$ , the resulting solution disperses at first, which means that the matter distributes more evenly in space and spacetime becomes flatter. This corresponds to an initial increase of  $e^{\mu(t,0)}$ ,  $\alpha(t,0)$ , or

$b(t, 0)$ , respectively. At least if  $y_0$  is not too large, we can clearly see that the solution starts reimploding at some point in time, which means that  $e^{\mu(t, 0)}$  decreases again, giving rise to an oscillating behavior. However, this oscillation occurs at values of  $e^{\mu(t, 0)}$  larger than  $e^{\mu(0, 0)}$ . We call this difference the initial elevation. As indicated in Section 4.2, the initial elevation can be observed for all  $y_0 > y_{\max}$ . These effects occur across all classes of steady states, types of perturbations promoting dispersion, and coordinate systems in a similar way and are illustrated in Figure 9 in the case of the King model in Schwarzschild coordinates for various  $y_0 > y_{\max}$ .

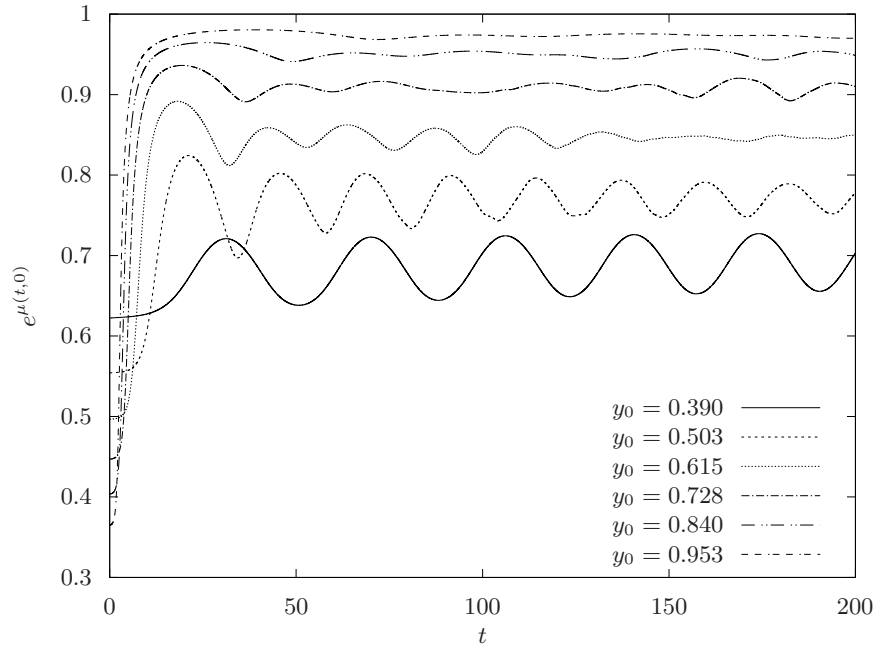


Figure 9: The King model in Schwarzschild coordinates for  $y_0 > y_{\max}$  perturbed by a dynamically accessible perturbation with direction  $\gamma > 0$ .

On the particle level we observe that during the initial dispersion, the particles spread in space. While some particles keep moving away from the spatial origin manifesting the initial elevation, a considerable amount returns after some time, which leads to a decrease of  $e^{\mu(t, 0)}$ , completing the first oscillation. This behavior of particles getting expelled and returning repeats several times until the system eventually oscillates around a seemingly unchanging configuration. In particular, the oscillating behavior cannot only be seen in  $e^{\mu(t, 0)}$ , but also on the particle level as well as in

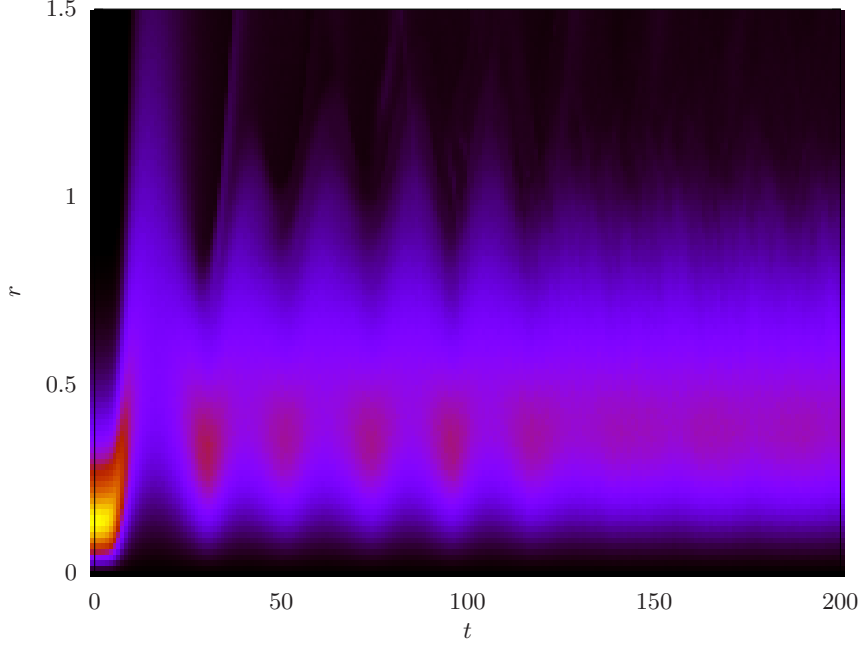


Figure 10: The weighted mass density  $4\pi r^2 \rho$  for the King model in Schwarzschild coordinates for  $y_0 = 0.6 > y_{\max}$  perturbed by a dynamically accessible perturbation with direction  $\gamma > 0$ . The color represents the value of  $4\pi r^2 \rho$ , increasing from black to yellow.

all metric and matter quantities. The oscillation of the mass density, i.e., the radial derivative of the Hawking mass, in the case of the King model is depicted in Figure 10.

Another illustration of the effect described above is given in Figure 11 where we plot the energy  $E$  of individual particles against their distance from the origin. Thereby, we can investigate trajectories of particles. Note that the scales of both the energy  $E$  and the radius  $r$  change from the plot for  $t = 0$  to the plot for  $t = 15$  and stay the same for  $t > 15$ . Plotting these specific quantities allows us to identify a portion of low energy particles that seems to form some dense structure which is independent of the less dense particles with higher energy. In addition, the dispersion of clusters of particles can be observed in both Figure 10 and 11.

A possible interpretation of these observations is that after perturbation a part of the solution corresponding to high energy particles disperses while after some transition period the remainder starts oscillating around a new

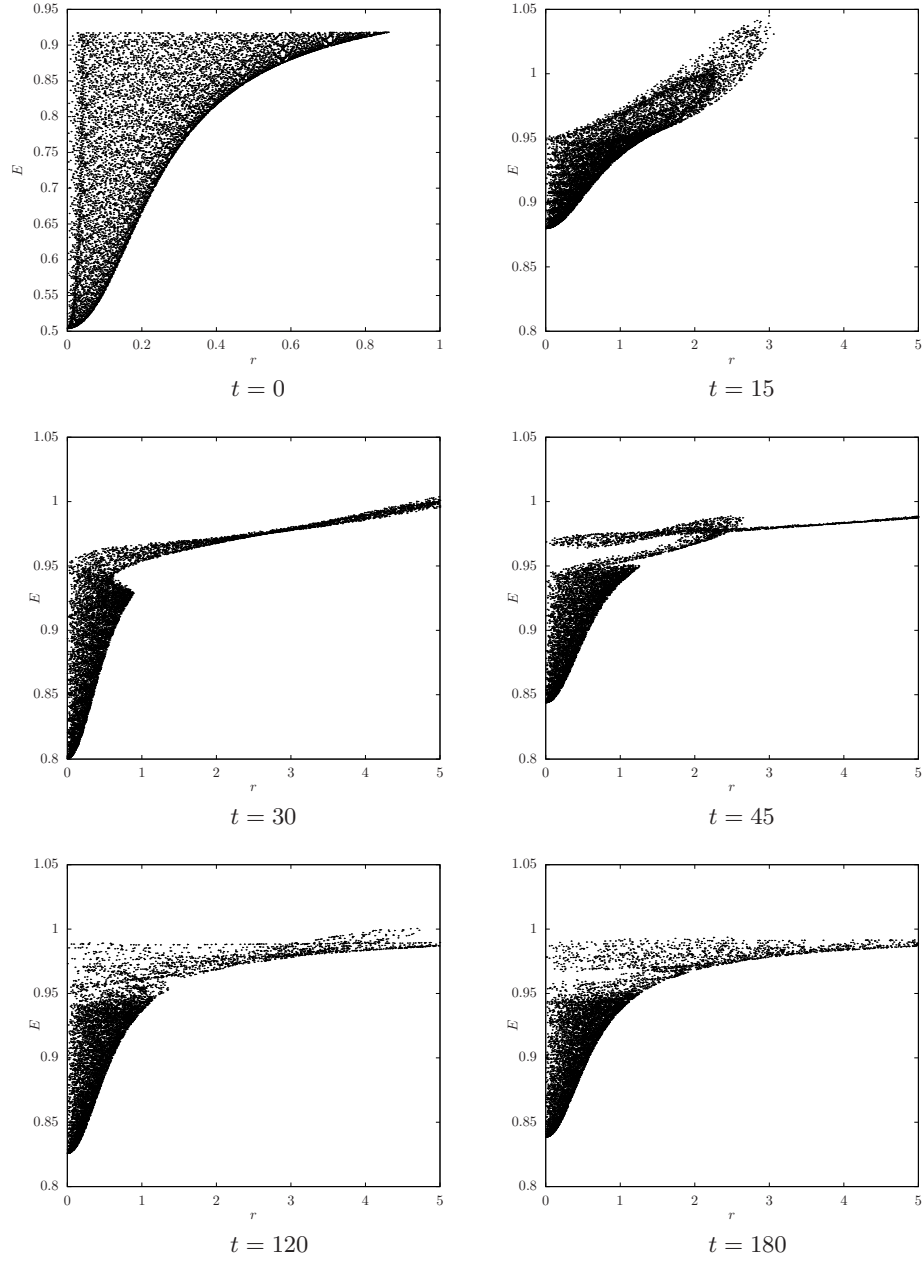


Figure 11: Numerical particles for the King model in Schwarzschild coordinates for  $y_0 = 0.6 > y_{\max}$  perturbed by a dynamically accessible perturbation with direction  $\gamma > 0$ . The movie corresponding to these snapshots is available at [31].

steady state. This new state is less relativistic than the original one and seems to depend solely on the original equilibrium, i.e., it is independent of numerical parameters and the type and strength of the perturbation used to perturb the original unstable steady state, at least for sufficiently weak perturbations. In the context of dynamical systems such a new state is usually a stable steady state of the system, and the above behavior is reminiscent of a heteroclinic orbit, as the original steady state after perturbation migrates to a different one. On the other hand, it does not really seem to converge towards this new state, as would be the case for a genuine heteroclinic orbit, so we use this terminology very loosely.

Since the Einstein-Vlasov system possesses a plethora of steady states, the explicit identification of the target state seems to be very delicate. We developed a method which acts on the level of particles and basically “deletes” all the “departed” particles from our solution before fitting the remainder by some stable steady state. However, a weak point of our procedure is that we have to decide manually whether or not a particle belongs to the “remainder”. In our simulations, we always made this decision based on the radius or the particle energy. All this being said the observations with the above procedure seem to support the “heteroclinic orbit picture”. Developing appropriate criteria for the latter question would definitely open up new possibilities for the search of these target states. In passing we note that Figure 11 actually presents snapshots from a movie which illustrates the above behavior and which, together with similar simulations, can be viewed via the link [31].

As can be seen in Figure 9, the difference between the value of  $e^{\mu(t,0)}$  around which the solution oscillates at later times and the initial value  $e^{\mu(0,0)}$  increases in  $y_0$ . In particular, the initial elevation also increases in  $y_0$ . This is caused by a relative increase of the number and mass of particles which initially get expelled from the configuration as well as a decrease of the number of particles which return. This difference seems to change smoothly in  $y_0$  which causes the initial elevation to be very subtle for  $y_0 \approx y_{\max}$ , cf. Figure 6, consistent with the fact that no such elevation occurs in the stable regime. Furthermore, the time-frame of the initial reimplosion of the solution increases rapidly in  $y_0$  when choosing  $y_0$  large enough, which means that the existence of fully dispersing solutions induced by large  $y_0$  can not be ruled out numerically.

It has been suggested in [28] that perturbations promoting dispersion of certain isotropic steady states with negative binding energy lead to fully dispersing solutions. In [3], this suggestion has been extended to non-isotropic steady states with an inner vacuum region, i.e.,  $L_0 > 0$ . However, our results

disprove this conjecture in all three coordinate systems under consideration. In the case of the King model, the binding energy of a steady state is negative for  $y_0 > 0.784$  which means that Figure 9 clearly shows the reimplosion and oscillation of solutions emerging from weakly perturbed steady states with negative binding energy. The same phenomenon can also be observed for other isotropic and non-isotropic models, at least if  $L_0$  is not too large. In the case of a polytropic ansatz with  $k = 0.5$ ,  $l = 0.1$ ,  $L_0 = 0.001$  this is depicted in Figure 12.

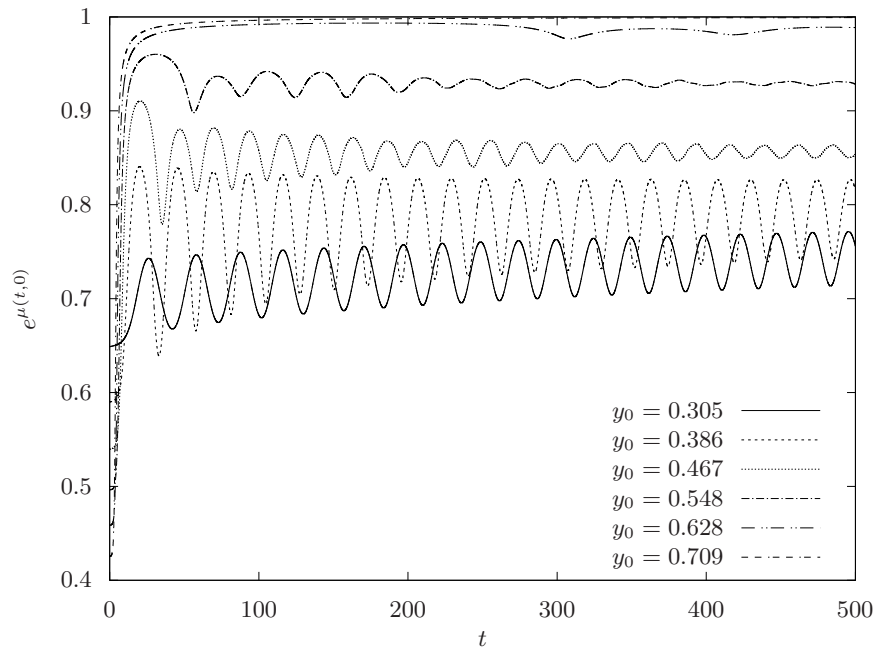


Figure 12: The polytropic ansatz with  $k = 0.5$ ,  $l = 0.1$ ,  $L_0 = 0.001$  in Schwarzschild coordinates with  $y_0 > y_{\max}$  perturbed by a dynamically accessible perturbation with direction  $\gamma > 0$ .

Notice that  $L_0$  is closely connected to the size of the inner vacuum region of steady states. Increasing this parameter in the ansatz function seems to slow down all occurring effects, in particular causing the reimplosion time to increase. This effect is the main reason why we choose  $L_0$  rather small. In fact, when setting  $L_0$  significantly larger, we cannot decide whether some steady states with  $y_{\max} < y_0 < y_{\text{zero}}$  reimplode or fully disperse. A similar effect can be observed for large  $k$ . Furthermore, large  $y_0$  pose a problem when examining dispersing steady states for every model since we cannot

numerically distinguish solutions with large reimplosion times from fully dispersing ones. It therefore remains an open question whether or not there exist fully dispersing solutions emerging from weakly perturbed unstable steady states and if this behavior is connected to the binding energy of the original steady states in some way.

## 5 Discussion of the numerics

We conclude our paper with an overview of the parameter settings which influence the numerical accuracy. Compared to former numerical projects in this field of research, we benefit from more computational power and from a parallelized code. This allows us to perform computations with a large number of numerical particles within a reasonable computation time. The actual computation time further depends on the discretization of the time variable  $t$  and the spatial variable  $r$ . We typically use  $\Delta r$  and  $\Delta t$  in the order of magnitude of  $10^{-4}$ . Moreover, we ensure that at least 15 million numerical particles are used for our computations by choosing the number of steps  $N_u$  and  $N_\psi$  suitably after fixing  $\Delta r$  and  $\Delta t$ . In order to guarantee that perturbations resulting of errors due to our initialization are small compared to our applied perturbation and that the applied perturbation is reasonably small we choose  $T_{pert} = 0.5$  and  $\epsilon_{pert}$  of the order  $10^{-4}$  and determine a suitable  $\gamma$  as described in Section 3.

To monitor the validity of our simulation, we keep track of the ADM mass  $M(t)$  and the analytical number of particles  $N(t)$  which are conserved quantities along solutions of the Einstein-Vlasov system. We define the relative errors as

$$e_M(t) = \frac{|M(t) - M|}{M}, \quad e_N(t) = \frac{|N(t) - N|}{N}$$

where  $M = M(T_{pert})$  and  $N = N(T_{pert})$  are given by the perturbed steady state, i.e., the evolved state at  $t = T_{pert}$ . In the case of oscillating or heteroclinic solutions the errors stay very small—of the order  $10^{-4}$  until  $t = 100$ —when choosing the numerical parameters as mentioned above. When considering the formation of a trapped surface and the formation of a black hole, it turns out that the errors become larger and—not surprisingly—the simulation eventually breaks down.

A further test of our codes is to evolve an unperturbed steady state. When choosing a stable steady state it is tracked faithfully for very long times. Obviously, for an unstable steady state the errors due to the initialization can eventually cause a deviation from the steady state. In conclusion,



it seems fair to say that our simulations provide conclusive results at least if we are not considering the long time behavior of collapsing solutions after trapped surfaces have formed.

## References

- [1] ANDRÉASSON, H., The Einstein-Vlasov System/Kinetic Theory. *Living Reviews in Relativity* **14**, 4 (2011).
- [2] ANDRÉASSON, H., KUNZE, M., REIN, G., Global existence for the spherically symmetric Einstein-Vlasov system with outgoing matter, *Comm. Partial Differential Eqns.* **33**, 656–668 (2008).
- [3] ANDRÉASSON, H., REIN, G., A numerical investigation of the stability of steady states and critical phenomena for the spherically symmetric Einstein-Vlasov system. *Class. Quantum Gravity* **23**, 3659–3677 (2006).
- [4] ANDRÉASSON, H., REIN, G. On the steady states of the spherically symmetric Einstein-Vlasov system. *Class. Quantum Gravity* **24**, 1809–1832 (2007).
- [5] ANDRÉASSON, H., REIN, G., The asymptotic behaviour in Schwarzschild time of Vlasov matter in spherically symmetric gravitational collapse. *Math. Proc. Camb. Phil. Soc.* **149**, 173–188 (2010).
- [6] ANDRÉASSON, H., REIN, G., Formation of trapped surfaces for the spherically symmetric Einstein-Vlasov system. *J. Hyperbolic Differ. Equ.* **7:4**, 707–731 (2010).
- [7] BISNOVATYI-KOGAN, G. S., ZEL'DOVICH, YA. B., Models of clusters of point masses with great central red shift. *Astrofizika*, **5**, 223–234 (1969).
- [8] GÜNTHER, S., The Einstein-Vlasov system in maximal areal coordinates. Master thesis, Bayreuth 2019.
- [9] HADŽIĆ, M., LIN, Z., Turning point principle for relativistic stars. Preprint, <https://arxiv.org/abs/2006.09749> (2020).
- [10] HADŽIĆ, M., REIN, G., Stability for the spherically symmetric Einstein-Vlasov system—a coercivity estimate. *Math. Proc. Camb. Phil. Soc.* **155**, 529–556 (2013).

- [11] HADŽIĆ, M., REIN, G., On the small redshift limit of steady states of the spherically symmetric Einstein-Vlasov system and their stability. *Math. Proc. Camb. Phil. Soc.* **159**, 529–546 (2015).
- [12] HADŽIĆ, M., LIN, Z., REIN, G., Stability and instability of self-gravitating relativistic matter distributions. Preprint, <https://arxiv.org/abs/1810.00809> (2018).
- [13] IPSER, J. R., Relativistic, Spherically Symmetric Star Clusters. III. Stability of Compact Isotropic Model. *Astrophys. J.* **158**, 17–43 (1969).
- [14] IPSER, J., A binding-energy criterion for the dynamical stability of spherical stellar systems in general relativity. *Astrophys. J.* **238**, 1101–1110 (1980).
- [15] IPSER, J., THORNE, K. S., Relativistic, spherically symmetric star clusters I. Stability theory for radial perturbations. *Astrophys. J.* **154**, 251–270 (1968).
- [16] LIN, Z., ZENG, C., Separable Hamiltonian PDEs and Turning point principle for stability of gaseous stars. Preprint, <https://arxiv.org/abs/2005.00973> (2020).
- [17] KORCH, M., RAMMING, R., REIN, G., Parallelization of Particle-in-Cell Codes for Nonlinear Kinetic Models from Mathematical Physics. *ICPP 13: Proceedings of the 2013 42nd International Conference on Parallel Processing*, 523–529 (2013).
- [18] I. OLABARRIETA, M. W. CHOPTUIK, Critical phenomena at the threshold of black hole formation for collisionless matter in spherical symmetry, *Phys. Rev. D.* **65**, 024007 (2002).
- [19] PENROSE, R., Gravitational Collapse and Space-Time Singularities *Physical Review Letters* **14.3**, 57–59 (1965).
- [20] RAMMING, R., REIN, G., Spherically symmetric equilibria for self-gravitating kinetic or fluid models in the nonrelativistic and relativistic case—a simple proof for finite extension. *SIAM J. Math. Analysis* **45**, 900–914 (2013).
- [21] RAMMING, R., REIN, G., Oscillating solutions of the Vlasov-Poisson system—A numerical investigation. *Phys. D* **365**, 72–79 (2018).

- [22] REIN, G., *The Vlasov-Einstein System with Surface Symmetry*, Habilitationsschrift, München 1995.
- [23] REIN, G., Collisionless kinetic equations from astrophysics—The Vlasov-Poisson system. In *Handbook of Differential Equations, Evolutionary Equations, vol. 3*, edited by C. M. Dafermos and E. Feireisl, Elsevier (2007).
- [24] REIN, G., RENDALL, A., Global existence of solutions of the spherically symmetric Vlasov-Einstein system with small initial data. *Commun. Math. Phys.* **150**, 561–583 (1992). Erratum: *Commun. Math. Phys.* **176**, 475–478 (1996).
- [25] REIN, G., RENDALL, A. D., SCHAEFFER, J., Critical collapse of collisionless matter: A numerical investigation. *Phys. Rev. D* **58**, 044007 (1998).
- [26] REIN, G., RODEWIS, T., Convergence of a particle-in-cell scheme for the spherically symmetric Vlasov-Einstein system, *Indiana University Math. J.* **52**, 821–862 (2003).
- [27] SCHAEFFER, J. Discrete approximation of the Poisson-Vlasov system. *Q. Appl. Math.* **45**, 59–73 (1987).
- [28] SHAPIRO, S. L., TEUKOLSKY, S. A., Relativistic Stellar Dynamics on the Computer—Part Two—Physical Applications. *Astrophysical Journal* **298**, 58 (1985).
- [29] ZEL'DOVICH, Y. B., PODURETS, M. A., The Evolution of a System of Gravitationally Interacting Point Masses. *Soviet Astronomy* **9**, 742–749 (1966).
- [30] ZEL'DOVICH, Y. B., NOVIKOV, I. D., Relativistic astrophysics. Vol.1: Stars and relativity. *Chicago: University of Chicago Press* 1971.
- [31] <http://www.diffgleichg.uni-bayreuth.de/en/research/einstein-vlasov-numerics/> (accessed September 18, 2020).